Design, Synthesis, Structural and Textural Characterization, and Electrical Properties of Mesoporous Thin Films Made of Rare Earth Oxide Binaries

Jessie Hierso,[†,‡] Ozlem Sel,[†,‡] Armelle Ringuede,[§] Christel Laberty-Robert,*[,†,‡] Luc Bianchi,[||] David Grosso,[†,‡] and Clément Sanchez*[,†,‡]

UPMC Univ Paris 06, UMR 7574, and CNRS, UMR 7574, Chimie de la Matière Condensée de Paris, F-75005, Paris, France, CEA-Le Ripault, Laboratoire SOL-GEL et Simulation, Département Matériaux, BP 16, 37260 Monts, France, and Laboratoire d'Electrochimie et Chimie Analytique, UMR 7575, CNRS, ENSCP, Paris6, 11 Rue Pierre et Marie Curie, F-75231 Paris Cedex 05, France

Received September 29, 2008. Revised Manuscript Received March 20, 2009

Ceria-based oxides are of interest as electrolyte and electrode materials in intermediate-temperature solid-oxide fuel cell (SOFCs). A sol−gel strategy has been developed for the production of mesoporous, nanostructured, single phase $Ln_{0.1}Ce_{0.9}O_2$, Ln = La, Y, Sm, Gd, Dy thin films. The ceria-based mesoporous thin films exhibit high specific area, periodic through-connected networks of mesopores (∼20 nm), and continuous networks of nonagglomerated nanoparticles (15 nm). Calcination at relatively mild temperature for this oxide (300 °C) converts the amorphous films to nanocrystalline fluorine $Ln_{0.1}Ce_{0.9}O_2$. Although densified during calcination, the mesoporous nanoarchitectures retain porosity, high surface area, and limited particle agglomeration. The electrical properties of mesoporous thin films are evaluated from 400 to 500 °C in air. The conductivity of these mesoporous thin films is comparable to the one observed for dense ceramic containing particles in the nanometer range, reflecting that the interparticulate junctions are not restrictive for the transport of oxide-ion vacancies. A high degree of interconnectivity has been established between the nanocrystallites (<15 nm) in these mesoporous thin films, yielding electroceramic films where the grain boundaries are not restrictive for the oxygen ion transport. This study provides processing guideline to achieve fabrication of 3-D mesostructured thin films for efficient interface in SOFC.

1. Introduction

Microsolid oxide fuel cells (μSOFCs) operating at temperatures of 300−600 °C are an interesting alternative to Li-ion batteries or Ni-metal hydride because they offer energy density and specific energy three to four times higher.[1−5] Unlike state-of-the-art SOFC, these systems exhibit a total thickness of, at most, 10 μm for the catalytically and electrochemically active layers. This feature imposes a change in the way the cell is designed. This includes materials selection and processing techniques.

Electrodes based on cerium oxide are promising for this application because of their efficient electrochemical activity. The unique electronic and electrochemical properties of CeO_2 is largely related to the ease in generating Ce(III) and Ce(IV), which can be tuned through the particle size. In its microcrystalline state, CeO_2 exhibits mixed conductivity at high temperature and/or under low-partial pressure of oxygen. As the size of the particles decreases, nanoceria expresses mixed electronic and ionic conductivities at low temperature under air. The electronic transport is promoted by the greater number of defects. Moreover, the degree of defects in an electrode material strongly affects the properties which are critical to the electrode performance: the transport of ionic and electronic carriers and the efficiency of the electrochemical reactions at the interfaces. These phenomena are well-known and have been reported for numerous materials.[7] For example, small crystallites of ceria into the porous YSZ layer are reduced at much lower values of $P(O_2)$ than required for bulk ceria, enhancing thus the electronic conductivity of the composite layer.[6] This electronic conductivity is sufficient to produce electrode functional layers with high performance. These innate properties of nanoceria-based materials may be further magnified with ceria produced in nanostructured forms.[7]

Mesoporous materials composed of metal oxides such as titania, ceria, and perovskites are classes of sol−gel derived

---

* Corresponding authors. E-mail: christel.laberty@upmc.fr (C.L.-R.); clement.sanchez@upmc.fr (C.S.).

[†] UPMC Univ Paris 06, UMR 7574.

[‡] CNRS, UMR 7574.

[§] UMR 7575, CNRS, ENSCP.

[||] CEA-Le Ripault.

(1) Perednis, D.; Gauckler, L. J. *Solid State Ionics* **2004**, *166*, 229–239.
(2) Bieberle-Hutter, A.; Beckel, D.; Infortuna, A.; Muecke, U. P.; Rupp, J. L. M.; Gauckler, L. J.; Rey-Mermet, S.; Muralt, P.; Bieri, N. R.; Hotz, N.; Stutz, M. J.; Poulikakos, D.; Heeb, P.; Muller, P.; Bernard, A.; Gmur, R.; Hocker, T. *J. Power Sources* **2008**, *177* (1), 123–130.
(3) Stoermer, A. O.; Rupp, J. L. M.; Gauckler, L. J. *Solid State Ionics* **2006**, *177*, 2075–2079.
(4) Rupp, J. L. M.; Gauckler, L. J. *Solid State Ionics* **2006**, *177*, 2513–2518.
(5) Beckel, D.; Bieberle-Hüttera, A.; Harvey, A.; Infortuna, A.; Muecke, U. P.; Prestat, M.; Rupp, J. L. M.; Gauckler, L. J. *J. Power Sources* **2007**, *173*, 325–345.
(6) Gorte, R. J.; Vohs, J. M.; McIntosh, S. *Solid State Ionics* **2004**, *175* (1−4), 1–6.
(7) Rolison, D. R.; Dunn, B. *J. Mater. Chem.* **2001**, *11*, 963–980.

10.1021/cm802627k CCC: $40.75

materials that are composed of bicontinuous networks of nanoscopic solid materials and mesopores. The inherent characteristics of such nanoarchitectures are highly beneficial for SOFC operation as a porous electrode structure is desirable for fast transport of ionic or electronic carriers through the solid phase, rapid flux of gases through the pores, and efficient electrochemical reactions at the interfaces. The benefit of nanostructured electrode architectures has recently been demonstrated for optimizing conductivity and electrocatalytic activity.[7−11] The polarization resistance was directly dependent on the particle size and the porosity of the ionic conductor.[11] The nanoarchitecture plays a pivotal role in maximizing the number of reactive sites and thus the catalytic activity of ceria-based catalysts for the electrochemical reaction of oxygen. Until now, no detailed studies have measured the impact of the porosity and grain size in the nanometer range of thin films of Ln-doped ceria on the electrical properties. This is however a very important issue to be able to use this approach in μ-SOFCs.

The synthesis of Ln-doped ceria thin films ($\leq 1\ \mu$m) has been previously achieved via spray-pyrolysis,[3,4,12] pulsed laser deposition,[13,14] e-beam technology,[15,16] chemical vapor deposition,[17] and atomic layer deposition (ALD).[18] Materials are dense and exhibit grains in the nanosize range. Additionally, in some techniques, it is difficult to obtain the correct stoichiometry. Few studies are focused on the preparation of meso-structured rare earth films and their properties, because of the difficulty of controlling the reaction rate of the hydrolysis and condensation reactions of trivalent cation.[19,20] Recently, Antonietti et al. developed a new type of diblock copolymer, where the two blocks, the hydrophilic block and the hydrophobic block, exhibit a high contrast. This block-copolymer was efficiently used for synthesizing mesoporous films containing trivalent or di-cations.[21−25] The synthesis of mesoporous rare earth doped Y_2O_3 and cerium thin films have then been achieved using amphiphilic poly(ethylene-*co*-butylene)-*b*-poly(ethylene oxide).[26] These films exhibit homogeneous pore-size distributions, with crystallite size tuned as a function of the heat treatment. However, no electrical measurements of these mesoporous thin films were reported. If these nanoarchitectures are to be explored for μ-SOFC applications, it is critical to understand their fundamental electrical properties, especially at relevant temperatures, which are typically $\geq$300 °C.

In this report, we describe the synthesis of mesoporous ceria-based thin films. Our approach is based on forming olygomer of Ce−O−Gd via thermo-driven hydrolysis and condensation reactions and combining it with a commercially available (PS-PEO) thermostable template. The electrical properties of these mesoporous architectures are reported and compared to the literature data obtained for dense ceramics. Our investigations demonstrate that the ionic conductivity of the mesoporous thin films is comparable to Gd-doped nanocrystalline ceria ceramic. Additionally, the oxygen ion diffusion or/and migration in these nanoarchitectures is fast and is not restricted by the particle−particle junction, indicating the existence of an uninterrupted three-dimensional (3D) pathway for ion conduction.

2. Experimental Procedures

Chemicals. $CeCl_3 \cdot 7H_2O$ (Aldrich, 99.999%), $GdCl_3 \cdot 6H_2O$ (Aldrich, 99.999%), $LaCl_3 \cdot 7H_2O$ (Aldrich, 99,999%), $SmCl_3 \cdot 7H_2O$ (Aldrich, 99.95%), polystyrene-*b*-polyethylene oxide (Polymer Sources Inc., P4750-SEO, polystyrene (40 000)-*b*-polyethylene oxide (45 000)), ethyl alcohol, and tetrahydrofuran (VWR, Normapur) were used as received.

Synthesis and Processing of Ln-CeO_2 MesoStructured Thin Films. Ln-doped ceria are prepared by modifications to our previously reported procedures for pure ceria.[24] To a solution of (0.665 g) $CeCl_3 \cdot 7H_2O$ and (0.075 g) $GdCl_3 \cdot 6H_2O$ in 5 mL of an ethyl alcohol and 0.75 mL of water, 100 mg of PS-*b*-PEO dissolved in ∼2.3 mL of tetrahydrofuran is added with stirring. The solution is then stirred for a minimal time of 1 h, to homogeneize the formation of the micelles in solution. After homogenization, the sol is constituted of spherical micelles (∼30 nm) surrounded by both hydrated Ce(III) and Gd(III) cations. In this approach, the hydrolysis and condensation reactions occur only during the heat treatment.[26]

The films were synthesized through the dip-coating approach. Substrates such as FTO, ceramics (YSZ, Al_2O_3), or conductive stainless steel were dipped in the as-described solutions and withdrawn with a speed of 2.2 $mm \cdot s^{-1}$. The atmosphere in the dip-coater is static dry air. The as-synthesized films were immediately heated in air at different temperatures (from 130 to 500 °C) for 15 min.

Physical Characterization. In situ thermal ellipsometry was used to analyze the thermal behavior of the as-synthesized mesostructured film.[27] Ellipsometer measurements were performed on a UV−vis

---

(8) de Souza, S.; Visco, S. J.; de Jonghe, L. C. *J. Electrochem. Soc.* **1997**, *144*, L35−L37.

(9) Kim, G.; Vohs, J. M.; Gorte, R. J. *J. Mater. Chem.* **2008**, *18*, 2386–2390.

(10) Kim, J. W.; Virkar, A. V.; Fung, K. Z.; Mehta, K.; Singhal, S. C. *J. Electrochem. Soc.* **1999**, *146*, 69–78.

(11) Zhen, Y. D.; Tok, A. I. Y.; Jiang, S. P.; Boey, F. Y. C. *J. Power Sources* **2008**, *178* (1), 69–74.

(12) de Jonghe, L. C.; Jacobson, C. P.; Visco, S. J. *Annu. Rev. Mater. Res.* **2003**, *33*, 169–182.

(13) Muecke, U. P.; Akiba, K.; Infortuna, A.; Salkus, T.; Stus, N. V.; Gauckler, L. J. *Solid State Ionics* **2008**, *178* (33−34), 1762–1768.

(14) Infortuna, A.; Harvey, A. S.; Gauckler, L. J. *Adv. Funct. Mater.* **2008**, *18* (1), 127–135.

(15) Pederson, L. R.; Singh, P.; Zhou, X. D. *Vacuum* **2006**, *80* (10), 1066–1083.

(16) Jong Hoon, J.; Gyeong Man, C. *Solid State Ionics* **2006**, *177* (11−12), 1053–1066.

(17) Meng, G. Y.; Song, H. Z.; Dong, Q.; Peng, D. K. *Solid State Ionics* **2004**, *175*, 29–34.

(18) Bernay, C.; Ringuede, A.; Colomban, P.; Lincot, D.; Cassir, M. *J. Phys. Chem. Solids* **2003**, *64*, 1761–1770.

(19) Grosso, D.; Boissiere, C.; Smarsly, B.; Brezesinski, T.; Pinna, N.; Albouy, P. A.; Amenitsch, H.; Antonietti, M.; Sanchez, C. *Nat. Mater.* **2004**, *3* (11), 787–792.

(20) Sanchez, C.; Boissiere, C.; Grosso, D.; Laberty, C.; Nicole, L. *Chem. Mater.* **2008**, *20* (3), 682–737.

(21) Brezesinski, T.; Fattakhova Rohlfing, D.; Sallard, S.; Antonietti, M.; Smarsly, M. *Small* **2006**, *2* (10), 1203–1211.

(22) Brezesinski, T.; Erpen, C.; Iimura, K.-i.; Smarsly, B. *Chem. Mater.* **2005**, *17*, 1683–1690.

(23) Brezesinski, T.; Antonietti, M.; Groenewolt, M.; Pinna, N.; Smarsly, B. *New J. Chem.* **2005**, *29* (1), 237–242.

(24) Brezesinski, T.; Smarsly, B.; Groenewolt, M.; Antonietti, M.; Grosso, D.; Boissiere, C.; Sanchez, C. *Stud. Surf. Sci. Catal.* **2005**, *156*, 243–248 (Nanoporous Materials IV).

(25) Wang, T.; Sel, O.; Djerdj, I.; Smarsly, B. *Colloid Polym. Sci.* **2006**, *285* (1), 1–9.

(26) Castro, Y.; Julian-Lopez, B.; Boissiere, C.; Viana, B.; Grosso, D.; Sanchez, C. *Microporous Mesoporous Mater.* **2007**, *103* (13), 273–279.

(27) Boissiere, C.; Grosso, D.; Lepoutre, S.; Nicole, L.; Bruneau, A. B.; Sanchez, C. *Langmuir* **2005**, *21* (26), 12362–12371.

variable-angle spectroscopic ellipsometer (VASA) from Woollam and data analysis was performed with the Wvase32 software. Measurements were fitted over the transparent range for ceria (400−1000 nm). The ellipsometer was fitted with a home-built covered heating unit connected to a programmable temperature regulator for thermal analyses. The calcination environment was adjusted by flowing 5 L·min^{-1} of gas through the sample stage at controlled relative humidity (RH).

Spectroscopic ellipsometry porosimetry (Woollam, U.S.A.) was used to characterize the pore size distribution and dimension. In this type of experiment, a dynamic flux of controlled humidified air is applied onto the mesostructured films. The humidity was adjusted using a mass flow controller and monitored using a relative humidity probe held in the environmental chamber. In this case, ellipsometry was conducted at room temperature (25 °C) using the adsorption−desorption isotherm of water analyzed with an isotropic inorganic pore contraction model and a modified Kelvin equation for ellipsoidal pores.

Ex situ infrared spectroscopy was used to analyze the mesostructured films calcined at various temperatures. The mesostructured Ln-CeO_2 films were mounted in a special cell allowing work in reflection mode. Spectra were collected under N_2 with a 25 scans at a resolution of 0.5 cm^{-1} and referenced to background spectra collected under the same condition.

XPS spectra were collected on a SPECS (Phoibos MCD 150) X-ray photoelectron spectrometer, using a Mg Kα ($h\nu = 1253.6$ eV) X-ray source having a 150 W (12 mA, 12.5 kV) electron beam power and a 7 × 2 mm spot size. The emission of photoelectrons from the sample were analyzed at a takeoff angle (θ) of 90° under ultrahigh vacuum conditions (10^{-8} Pa). High-resolution images were collected at a pass energy of 10 eV for C 1s, O 1s, Ce 3d, and Ln 3d core XPS levels. No charge compensation was applied during acquisition. After collection, the binding energies were calibrated with respect to the C 1s at a binding energy of 284.8 eV. The peak areas of the spectra were determined after subtraction of a Shirley background. The atomic ratio calulations were performed after normalization using Scofield factors. All spectra processing was carried out using the Casa XPS software package. The spectral decomposition was performed by using Gaussian functions after background subtraction.

Electron Microscopy. A JEOL JEM 2010 (200 kV) transmission electron microscope (TEM) equipped with a Gatan CDD camera was used to characterize the Ln-doped ceria mesostructured thin films, confirm particle size, and determine crystal structure. Samples were prepared by scratching the mesostructured films, wet-grinding the scratched films, and then depositing a drop of the solution onto holey-carbon film supports. We examine multiple areas of order 100 μm × 100 μm from each sample to ensure that the images obtained are representative.

Scanning electron microscopy (SEM, S440 LEICA) was used to characterize the surface and the thickness of Ln-CeO_2 mesostructured thin films. For analysis, the specimen was prepared by attaching a small portion of the mesostructured films to an aluminum stub using conductive carbon tape. The specimen was gold sputter-coated prior to analysis.

X-ray Diffraction. The Ln-CeO_2 films were analyzed using a bruker D8 Advance X-ray diffractometer. A 2θ survey scan performed from 20° to 60° at 1°/min and a sample interval of 0.05°. The particle size was evaluated using the Scherrer formula, eliminating machine broadening and the Cu K2α peak. An analysis at low angle was performed to characterize the mesostructure. A θ scan was performed from 0.5 to 4° at 1°·min^{-1} and a sample interval of 0.5°.

Electrical Properties. Impedance data were collected from 1 MHz to 0.1 Hz with a sampling interval of 11 per decade (frequency analyzer, autolab PGSTAT30) with 100 mV ac signal amplitude (ΔV) and no dc polarization for 500 °C-calcined ceria-based mesostructured thin films. The ceria-based mesostructured thin films were deposited on conductive stainless steel (Goodfellow, AISI 316) substrates. The ceria-based mesostructured films were held in a spring-loaded conductivity cell comprising ceramic tubes and ceramic plates using a platinum grid as the counter electrode and punctual platinum as the working electrode and the current collector.[18] With respect to the system linearity, a 100 mV ac signal amplitude (ΔV) was applied, without DC polarization. Conductivity cells were placed in an alumina tube (50 mm inside diameter) furnace and heated under static air. To determine the activation energy of electrical conduction, measurements were made in 20 °C intervals betweens 400 and 520 °C; the furnace was ramped between each temperature and allowed to equilibrate for 1 h before each measurement.

3. Results and Discussion

Thermal Processing and Characterization of Ln-CeO_2 Mesoporous Thin Films. As most of the applications of ceria-based materials require high-temperature operation (300−900 °C), we examined the effects of various thermal treatments on these porous Gd-CeO_2 nanoarchitectures. The as-synthesized Gd-CeO_2 thin films (heated at 130 °C, 2 h) were examined using in situ thermal ellipsometry (Figure 1). This analysis is used to elucidate the change on the thermally driven densification, pyrolysis, crystallization, and sintering of mesoporous thin films.[28] Through this technique, we determine the temperatures necessary to dehydrate, decompose the PS-*b*-PEO block copolymer, and crystallize the nano-Gd-doped ceria (Figure 1). These experiments consisted of recording the evolution of the films' refractive index and thickness as it is heated in air.[28] The variation of the films' refractive index and thickness as a function of the temperature is plotted in Figure 1b,c. The ellipsometric behavior for the Gd−ceria thin film is complex. This is due to dehydration, decomposition of adsorbed species, decomposition of template, crystallization of the Gd-CeO_2 nanoparticle, and evolution of the porous structure upon crystallization (Figure 1). Templated Gd-CeO_2 films exhibit a decrease in the index of refraction between 20 °C and 200 °C while the thickness of the film is almost constant. This little change in thickness was also observed by SEM-FEG analyses. The as-prepared film exhibits thickness comparable to the one heat-treated at 200 °C (not shown). As the temperature involved is low and the templated film exhibits high surface area, this step is attributed to the loss of physisorbed water. Upon further heating in air, the trace of the index of refraction of the Gd-CeO_2 template film reveals a feature between 200 °C and 300 °C. We observe a decrease in the refractive index and in the film thickness. Bass et al. have demonstrated the interest and the limits of this new technique to follow the complex evolution of mesoporous thin layers when submitted to a thermal treatment.[28,29] They

---

(28) Bass, J.; Boissiere, C; Grosso, D.; Sanchez, C.; Nicole, L. *J. Am. Chem. Soc.* **2008**, *130* (25), 7882–7897.

(29) Bass, J. D.; Boissiere, C.; Nicole, L.; Grosso, D.; Sanchez, C. *Chem. Mater.* **2008**, *17*, 5550–5556.

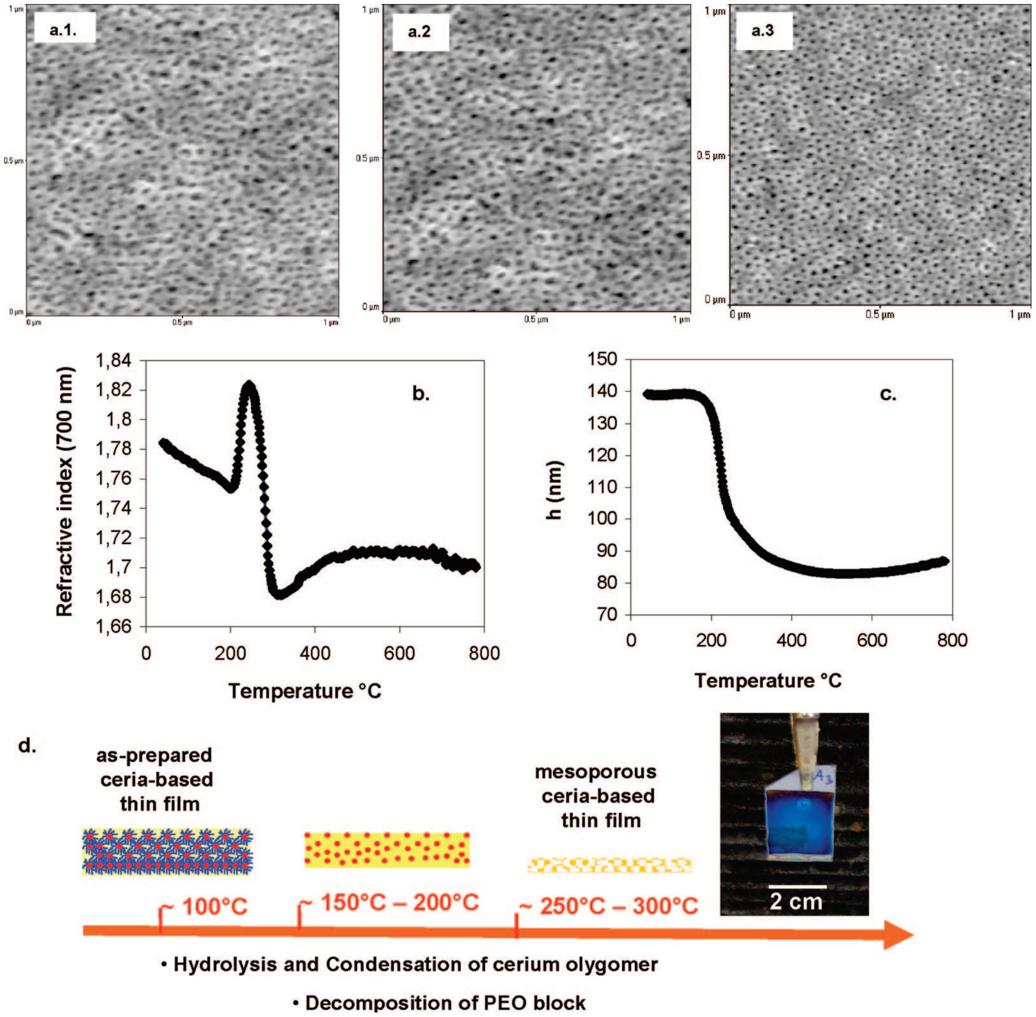

Figure 1. (a) AFM images of a mesoporous Gd-CeO$_2$ thin films calcined at various temperatures: (a.1) 220 °C, (a.2) 350 °C, and (a.3) 500 °C. (b) Variation of the refractive index (700 nm) as a function of the temperature, (c) variation of film thickness as function of the temperature for the as-synthesized Gd-CeO$_2$ mesoporous thin films, and (d) principle of the synthesis and proposed mechanism of Gd-CeO$_2$ mesoporous thin films formation.

have shown that a decrease in the index of refraction while the film contracts corresponds to the decomposition of the PEO and PS groups of the block-*co*-polymer, conducive to the formation of mesostructured films. Accordingly, we attributed this event to the formation of pores in the Gd-CeO$_2$ thin layers. This is supported by ex situ FTIR spectroscopy (Figure 2), AFM, and SEM-FEG analyses. Ex situ FTIR measurements show that residual organics and physisorbed water are eliminated after heating the Gd-CeO$_2$ thin films at 300 °C in air for 5 min. The δ-CH$_2$ stretching mode at 750 cm^{-1} and 900 cm^{-1} disappear after calcination at 300 °C. Additionally, the Ce−O−C vibration stretch at 676 cm^{-1} disappears after heat treatment at 300 °C. These vibrations correspond to the formation of carbonate species. Carbonated species are formed during the decomposition of the diblock copolymer. This formation is often observed during templated removal of transition or lanthanide metal oxide mesoporous materials. Additionally, the formation of the mesoporous network is confirmed by AFM and SEM-FEG analysis (Figures 1 and 3), where a mesoporous network is found for the Gd-CeO$_2$ thin film heat-treated at 220 °C and 300 °C. Around 300 °C, an increase of the refractive index is observed with a smooth decrease in the film thickness. According to Bass et al. this event corresponds to the transition from amorphous to crystalline oxide. This is supported by TEM electron diffraction that shows the formation of crystalline Gd-CeO$_2$ nanoparticles at 300 °C

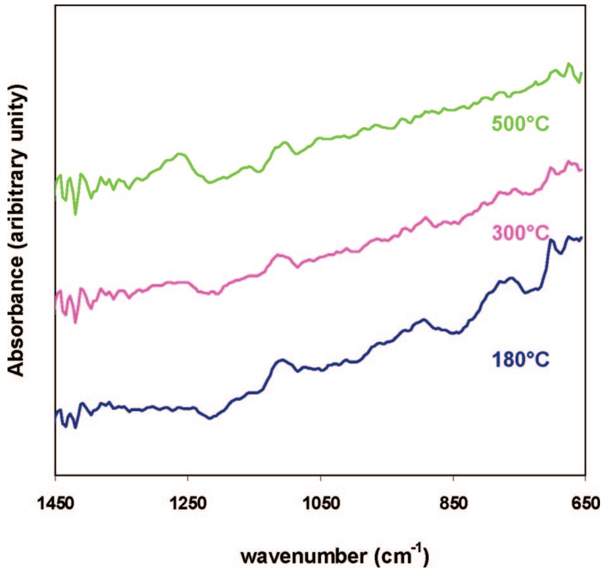

Figure 2. FTIR spectra for CGO thin films calcined at 180, 300, and 500 °C.

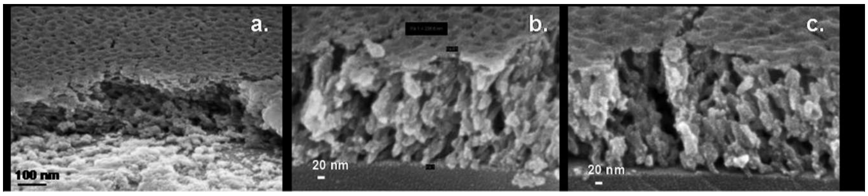

Figure 3. SEM-FEG images for Gd-CeO_2 samples calcined at various temperatures: (a) 300 °C, (b) 400 °C; and (c) 500 °C.

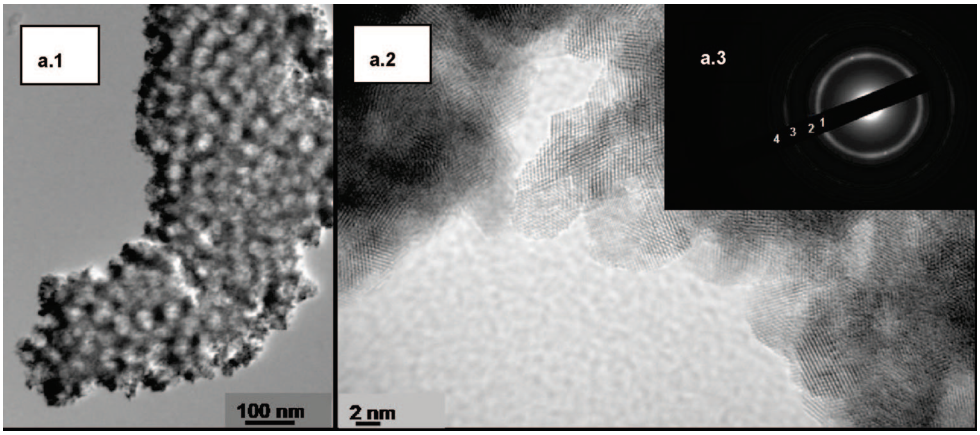

Figure 4. Transmission electron microscopy images and electron diffraction patterns for mesoporous thin films calcined at 300 °C (a.1; a.2, a.3); the materials are indexed to the cubic fluorite structure: (a.3) [1 (111); 2 (200); 3 (220); 4 (311)].

(Figure 4). This increase in the refractive index continues up to 500 °C. This event corresponds to a consolidation of the nanoscale ceria network. A slight decrease in the refractive index occurs between 600 and 800 °C. This change may be explained by a densification of the porous network. SEM-FEG images reveal a change in the pore structure. Heating the mesoporous film conduces to an evolution of the pore structure with the formation of pores open to the surface and connected in a direction perpendicular to the substrate surfaces or the film layer, forming a 3-D pores network (Figure 3).

Generally, templated porosity allows densification of oxide to occur in the $X-Y$ directions, parallel to the film surface, reducing the thickness of walls and generating porosity. Such interesting modification of the porous network, already observed in the case of TiO_2 mesoporous thin films, [28,30] corresponds to a rearrangement of pores due to the densification of the ceria-based matrix. This rearrangement allows the formation of a "porous channel" perpendicular to the surface of the substrates.

The Gd-doped ceria nanoarchitecture calcined at 300 °C exhibits networks of nanocrystalline particles of 6−7 nm in size and a network of mesopores (Figure 4). The microstructure of the Gd-doped ceria nanoarchitecture is highly porous and uniform, as evidenced by the results of the H_2O adsorption studies (Figure 5). The adsorption/desorption isotherms for the Gd-doped ceria nanoarchitecture after calcinations at 300 °C are shown in Figure 5. The nanoarchitecture has an isotherm consistent with mesoporosity and exhibits type-4 isotherms with H3-type hysteresis loops (Figure 5a). The pore volume of the Gd-doped ceria nanoarchitecture calcined at 300 °C is distributed over a broad range of pore sizes (up to 20 nm) with a volume-weight peak at approximately 10 nm (Figure 5b) which is the average diameter expected with the polystyrene (40 000)-*b*-polyethylene oxide (45 000). [28] This value agrees with the one evaluated from the treatment of AFM images (see Supporting Information).

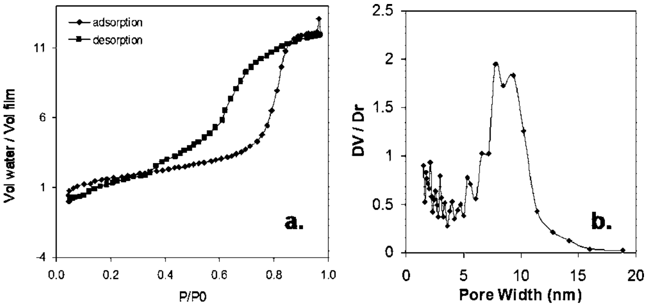

Figure 5. (a) Water adsorption/desorption isotherms of calcined Gd-CeO_2 nanoarchitectures at 300 °C. (b) Pore size distribution plots derived from H_2O-adsorption isotherms of calcined Gd-CeO_2 nanoarchitectures at 300 °C.

Calcining the Gd-CeO_2 nanoarchitecture at a temperature of relevance for SOFC operation (500 °C) does affect slightly the pore volume and the pore-size distribution (the volume-weight peak is about 15 nm), without subsequent change in the particles size (see Figures 6 and 7). A broader pore-size distribution with the formation of an interconnected pore array is observed for Gd-CeO_2 nanoarchitecture heat-treated at 500 °C, as seen in the SEM-FEG images (Figure 3) The Gd-CeO_2 at 500 °C contains pores open to the surface and connected in a 3-D network. The calcined $Gd_{0.1}Ce_{0.9}O_2$ films retain the mesostructure at 500 °C (Figure 6).

---

(30) Grosso, D.; Soler-Illia, G. J. A. A.; Crepaldi, E. L.; Cagnol, F.; Sinturel, C.; Bourgeois, A.; Brunet-Bruneau, A.; Amenitsch, H.; Albouy, P. A.; Sanchez, C. *Chem. Mater.* **2003**, *15*, 4562–4570.

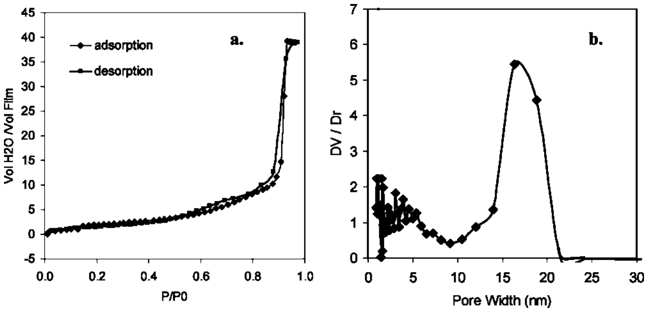

Figure 6. (a) Water adorption/desoption isotherms of calcined Gd-CeO_2 nanoarchitectures at 500 °C. (b) Pore size distribution plots derived from H_2O-adsorption isotherms of calcined Gd-CeO_2 nanoarchitectures at 500 °C.

The mesostructure for different doping, La and Y (see Supporting Information), has been also studied via X-ray diffraction and transmission electron microscopy analyses. The 1D SAXS exhibit a second-order reflection for crystallized La and Y doped-ceria heat-treated at 500 °C, suggesting for these samples a high degree of mesostructural order. The TEM images show that the Gd-CeO_2 thin films are constituted of nanoparticles and mesopores.

The calcination at 500 °C does not induce growth of the networked particles in Gd-CeO_2 samples, as seen in the transmission electron microscopy (TEM) images (Figure 7.).

As shown by TEM and SEM-FEG experiments, the calcined $Gd_{0.1}Ce_{0.9}O_2$ nanoarchitectures exhibit heavily faceted ~7−8 nm particles, surrounding pores of ~15 nm. This pore size is larger than the crystal size, which guarantees to some extent the stability of the mesopore framework. However, the calcination at 700 °C induces a consequent growth of the networked particles (~15 nm) which destroy the mesopores structure. These mesostructured Gd-doped CeO_2 films show high promise for application involving temperature up to 500 °C. Analysis of the lattice fringes yields *d*-spacings that match the cubic fluorite-type structure of Gd-doped ceria reported in the literature and the Joint Committee on Powder Diffraction Standards crystal database (card no. 75-0162).

The crystallographic structure of the calcined nanoarchitectures was further examined by using X-ray diffraction (XRD) (Figure 8). The diffraction peak is broad compared to microcrystalline Gd-CeO_2, confirming the nanocrystalline nature of the samples; the average particle size, determined by using the Scherrer equation for the Gd-CeO_2 (~10 nm), compares the particle size distribution seen for this nanoarchitecture by TEM analysis.

X-ray photoelectron spectroscopy (XPS) was used to ensure that Gd susbtitute Ce and further stabilize cerium exclusively as Ce^{4+} (Figure 9). The binding energies of the Ce 3d peak confirm the presence of a Ce(IV) oxide, with a small amount of Ce(III). However, the Ce 3d peaks are relatively sensitive to changes in oxidation state. The origin of Ce(III) can be due to partial reduction of Ce(IV) to Ce(III) during the XPS experiments.[31−34] The relative areas of Ce(III) and Ce(IV) peaks were used to calculate the average Ce oxidation state in the Gd-doped ceria films and yield 10%. This relatively small change in the Ce oxidation state corresponds to the cerium exclusively as Ce^{4+}, which is consistent with wide angle X-ray patterns. We further examined the O 1s photoelectron line. The positions of the binding energies are consistent with those of CeO_2 and CeO(OH), indicating the presence of hydoxyl group on the Gd-doped ceria mesostructured films. The relative areas of the Ce 3d and Gd 3d were used to calculate the Gd/Ce experimental ratio as 0.17. This relatively small change in the Ce/Gd ratio compared to the theoretical one (0.12) corresponds to a slight segregation of Gd ions at the surface. We, further, examined the Gd/Ce ratio by EDS analysis. The value of 0.10 ± 0.01 compared well with the theoretical value, confirming that the composition in the Gd-doped ceria film is uniform.

Electrical Properties of Gd-Doped Ceria Mesoporous Thin Films. The electrical properties of these mesostructured ceria-based nanoarchitectures were measured under air over the temperature range 400−500 °C. Representative impedance spectra obtained at various temperatures are presented in Figure 10.

The impedance spectrum of the Gd-doped ceria mesoporous thin film exhibits two features over the frequency range 1 MHz−0.01 Hz: an incomplete semi-circle at high frequency and a well-defined semicircle at low frequency. The size of the low-frequency impedance features scales with the signal amplitude, confirming that this spectral feature arises from the electrode response. Modifying the signal amplitude is like changing the oxygen partial pressure. If the impedance is a function of oxygen partial pressure, this is due to an important electronic conduction in the material, while an absence of variation reflects the ionic conductivity domain of the material. Note that, in our experimental conditions, the semi-circle at high frequency is not totally described. Higher frequencies would be required to totally define it.

The process occurring at high frequency has a resistance (intercept of the high frequency semi-circle with the Z' axis) decreasing from ~33 000 Ω at 400 °C to 3200 Ω at 520 °C. Because our 3-D nanoarchitecture exhibits a particle size of 15 nm, the resulting impedance can be reasonably modeled with a single semicircle, indicating that only one process dominates the impedance response.[35]

Indeed, as the particle size is reduced to the nanometer regime, the distinction between bulk and grain boundary regions tends to diminish, and the bulk contribution to the impedance response becomes more dominant.[35,49,50] We assigned this feature to a bulk conduction process. This process has a capacitance of 6.7×10^{-11} F, assigned to the bulk impedance.[36] Taking into account the film thickness (~270 nm) and the Pt punctual electrode contact surface (~2×10^{-3} cm^2),[37,38] we evaluated the conductivity of the Gd-

---

(31) Darnyanova, S.; Pawelec, B.; Arishtirova, K.; Huerta, M. V; Martinez, Fierro, J. L. G. *Appl. Catal. A* **2008**, *337* (1), 86–96.

(32) Romeo, M.; Bak, K.; Elfallah, J.; Lenormand, F.; Hilaire, L. *Surf. Interface Anal.* **1993**, *20* (6), 508–512.

(33) Francisco, M. S. P.; Mastelaro, V. R.; Nascente, P. A. P.; Florentino, A. O. *J. Phys. Chem. B* **2001**, *105* (43), 10515–10522.

(34) Ramirez-Cabrera, E.; Atkinson, A.; Chadwick, D. *Appl. Catal. B* **2002**, *36* (3), 193–206.

(35) Maier, J. *Solid State Ionics* **2002**, *148*, 367–374.

(36) Basu, S.; Sujatha, P.; Maiti, H. S. *J. Mater. Res.* **2004**, *19*, 3162–3171.

(37) Brahim, C.; Ringuede, A.; Cassir, M.; Putkonen, M.; Niinisto, L. *Appl. Surf. Sci.* **2007**, *253* (8), 3962–3968.

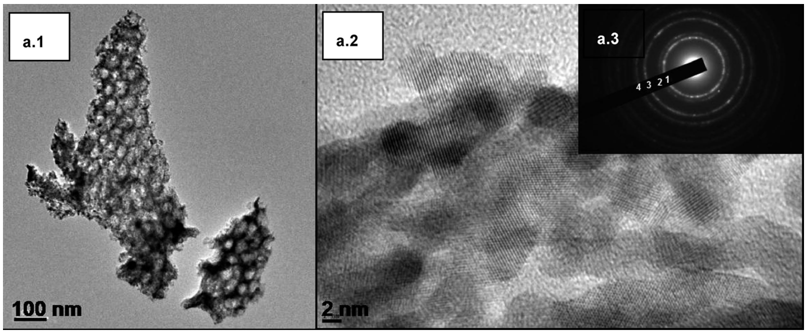

Figure 7. Transmission electron microscopy images and electron diffraction patterns for mesoporous thin films calcined at 500 °C (a.1, a.2, a.3) and 500 °C (a.1, a.2, a.3); the materials are indexed to the cubic fluorite structure: (a and b) [1 (111); 2 (200); 3 (220); 4 (311)].

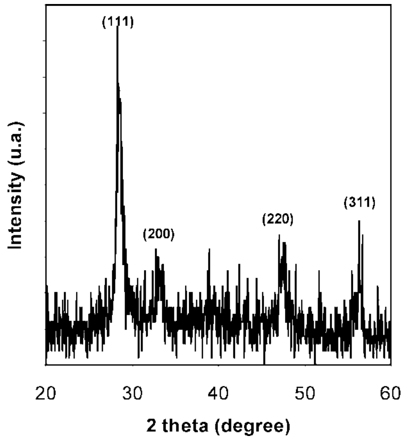

Figure 8. Wide angle X-ray diffractograms of the CGO mesoporous thin film (h = 300 nm), obtained after annealing at 500 °C.

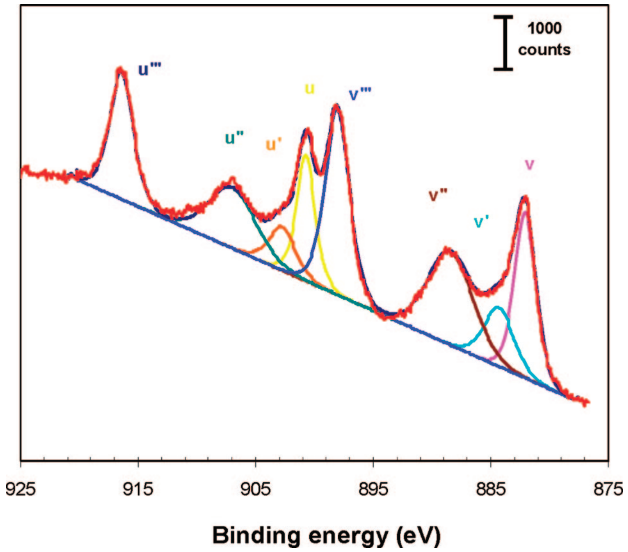

Figure 9. XPS spectra of mesostructured Gd-doped ceria thin film in the Ce 3d region.

doped ceria mesoporous thin film. Gd-doped ceria thin films have an ionic conductivity of 4×10^{-6} S·cm^{-1} at 520 °C.

Our experimental setup allows for through-plane electrical conductivity. However, other authors [35−39] reported for dense nanometric Gd-doped ceria ceramic bulk conductivity of 10^{-6} S/cm. Obtaining a conductivity value in this range for our Gd-CeO$_2$ nanoarchitectures reflects the presence of facile transport pathways for oxygen-ion vacancies. Furthermore, the interparticulate junctions and/or grain boundaries seem not to be an issue for restricted transport of oxygen-ion vacancies. This result agrees with the ones reported by Laberty et al. on various porous 3-D nanoarchitectures such as aerogel, ambigel, and xerogel for Gd-doped ceria, where the blocking grain boundary effect was found to be small.[49,50] Note that some discrepancy arises when comparing electrical data. This is mostly correlated to the method of measuring electrical conductivity, in-plane or through conductivities. For example, a conductivity value of 2 orders of magnitude higher has been recently reported for dense Gd-doped ceria thin films with particle size of 56 nm.[4] This value corresponds to in-plane conductivity.

Moreover, the activation energy, E_a, from Arrhenius plots in the low-temperature explored region (400 °C $\leq T \leq$ 520 °C) is 0.90 eV for mesoporous Gd-CeO$_2$ thin films. This value compares well the literature data.[40−42] Anselmi et al. [42] measured activation energy of 1 eV on nanometric highly doped ceria, and they assigned it to bulk conductivity, excluding the grain-boundary contribution. This result confirms that in our nanometer-scale material one transport dominates and indicates that facile transport occurs through this nanoarchitecture. Additionally, this result emphasizes that particle−particle junctions are not an issue for oxide-ion vacancies to migrate or/and diffuse through the 3-D nanoarchitecture. Further, the uninterrupted three-dimensional (3D) solid network exhibits sufficient percolation. The disappearance of the grain-boundary blocking effect has been already reported in bulk nanomaterials (particle size ~ 10 nm) with pure ionic conductivity.[44−48] Guo et al.[43]and Aoki

---

(38) Brahim, C; Ringuede, A; Gourba, E; Cassir, M; Billard, A; Briois, P. *J. Power Sources* **2006**, *156* (1), 45–49.

(39) Tschöpe, A.; Sommer, E.; Birringer, R. *Solid State Ionics* **2001**, *139*, 255–256.

(40) Jo, S. H.; Muralidharan, P.; Kim, D. K. *Solid State Ionics* **2008**, *178* (39−40), 1990–1997.

(41) Kim, S.; Maier, J. *J. Electrochem. Soc.* **2002**, *149* (10), J73−J83.

(42) Anselmi-Tamburini, U.; Maglia, F.; Chiodelli, G.; Tacca, A.; Spinolo, G.; Riello, P.; Bucella, S.; Munir, Z. A. *Adv. Funct. Mater.* **2006**, *16*, 2363–2368.

(43) Guo, X.; Zhang, Z. *Acta Mater.* **2003**, *51*, 5123–5130.

(44) Anselmi-Tamburini, U.; Garay, J. E.; Munir, Z. A.; Tacca, A.; Maglia, F.; Chiodelli, G.; Tacca, A.; Spinolo, G.; Riello, P.; Bucella, S.; Munir, Z. A. *Adv. Funct. Mater.* **2006**, *16*, 2363–2368.

(45) Chiodelli, G.; Spinolo, G. *J. Mater. Res.* **2004**, *19*, 3263–3269.

(46) Hwang, J. H.; Mclachlan, D. S.; Mason, T. O. *J. Electroceram.* **1999**, *3*, 7–16.

(47) Aoki, M.; Chiang, Y. M.; Kosacki, I.; Lee, J. R.; Tuller, H.; Liu, Y. *J. Am. Ceram. Soc.* **1996**, *79*, 1169–1180.

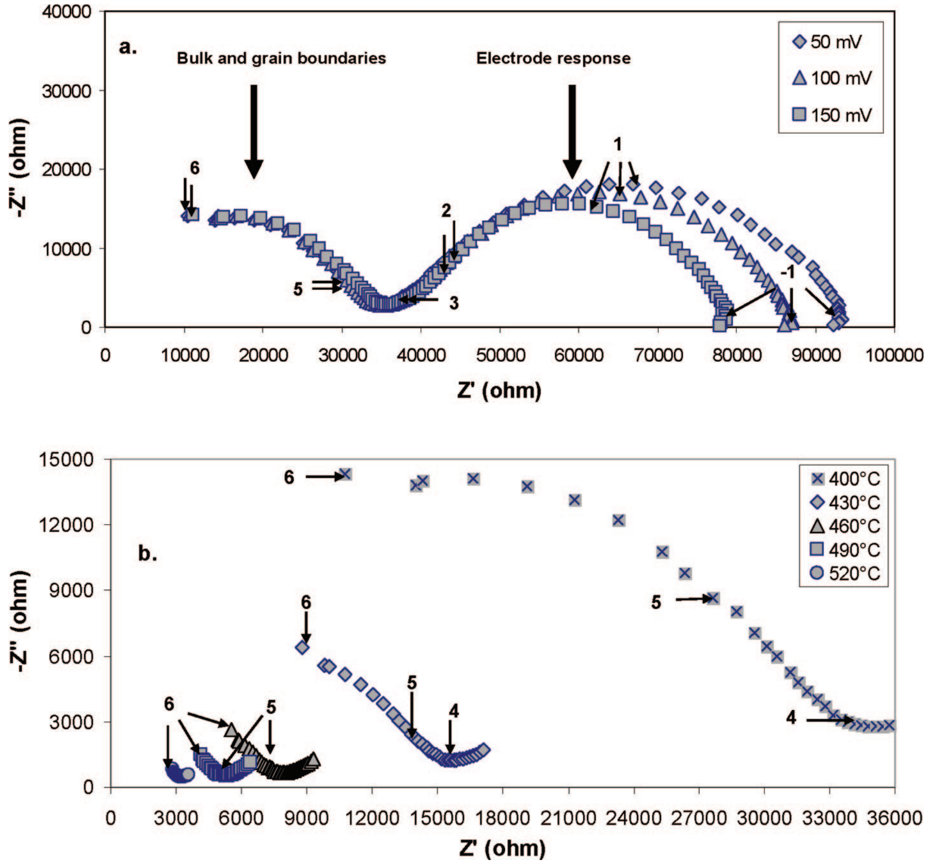

Figure 10. (a) The complex impedance spectrum at 400 °C in air of mesoporous Gd-doped ceria nanoarchitectures at various ΔE values. (b) Complex impedance diagram of Gd-doped ceria nanoarchitectures at various temperatures in air. Note that the contribution of the electrode is distinguished in the low-frequency arc. Film thickness: 270 nm.

et al.[47] reported similar observations for yttria-based zirconia ceramics exhibiting grain size in the nanometer range. On the basis of these literature data, we assume that a disappearance of the grain-boundary blocking effect is observed for dense ceramics with very small grain size and a constant dopant distribution in the grain boundary. In our Gd-doped ceria 3-D nanoarchitecture, the low grain-boundary blocking effect is attributed to the high "quality" of the grain boundary region. XPS and EDX analysis point out a slight increase in the substitutional atoms (GdCe′) leading to an increase of the oxygen vacancies in the proximity of the grain-boundary core. As the temperature used in our process is low (~500 °C) and the width of the grain boundary region is small, we can consider a uniform dopant distribution across the grain boundary, which in turn nullifies the blocking effect of the grain boundary. Because we plan to fabricate a solid-oxide fuel cell in which a mesoporous nanoscopic Gd-based ceria film resides at the interface, we limited our study to the electrical characterization of mesoporous based ceria-thin films.

Our sol−gel protocol can be readily adapted to prepare composite materials or additional mixed metal oxides with complex formulations. By adding colloidal solids to the Gd-doped ceria sol, composite nanoarchitectures are formed that retain the properties of each component. By analogy with previous studies,[51] composite structures composed of electroactive materials such as Sr-doped $LaMnO_3$ and 3-D ceria based mesoporous thin films will contain optimized three-boundary catalytic sites for use as SOFC anodes.

4. Conclusions

Mesoporous nanocrystalline ceria doped oxide nanoarchitecture thin films that retain the significant porosity characteristic of the bicontinuous pore-solid networks have been synthesized and characterized. The electrical transport properties in these nanoarchitectures show appealing behavior, related to their nanoparticles and their good particle/particle junctions. The present study emphasizes that creating nanoarchitectures with connected, interpenetrating pore and solid networks is critical in the effort to optimize electrical properties of nanostructured conductive materials for rate-critical applications. We are currently exploring new combinations and compositions of pore-solid architectures with the goal of achieving electrode structure that exhibit stability, high ionic conductivity when used as interfaces in solid-oxide fuel cells.

---

(48) Chiodelli, G.; Malavasi, L.; Massarotti, V.; Mustarelli, P.; Quartarone, E. *Solid State Ionics* **2005**, *176* (17−18), 1505–1512.

(49) Laberty-Robert, Ch.; Long, J. W.; Lucas, E. M.; Pettigrew, K. A.; Stroud, R. M.; Doescher, M. S.; Rolison, D. R. *Chem. Mater.* **2006**, *18*, 50–58.

(50) Laberty-Robert, Ch.; Long, J. W.; Pettigrew, K. A.; Stroud, R. M.; Rolison, D. R. *Adv. Mater.* **2007**, *19* (13), 1734–1739.

(51) Pietron, J. J.; Stroud, R. M.; Rolison, D. R. *Nano Lett.* **2002**, *2*, 545–549.

Acknowledgment. Financial support for this work was provided by the Laboratoire de Recherche Correspondant, CEA et Université Paris VI. J.H. is a Ph.D. student financed by the LRC. We would like to thank Sandra Cassale for the TEM images, Christophe Méthivier at the "Laboratoire de Réactivité des Surfaces" for the XPS measurement, and David Lantiat for SEM-FEG and AFM images analyses.

Supporting Information Available: Wide angle X-ray diffractograms, TEM images, electron diffraction patterns, AFM image, SEM-FEG image, and hisograms of pore size (PDF). This material is available free of charge via the Internet at http://pubs.acs.org.

CM802627K